

Flow of Moreno Glaciar, Argentina, from repeat-pass Shuttle Imaging Radar images: Comparison of the phase correlation method with radar interferometry

Remi Michel and Eric Rignot

Jet Propulsion Laboratory, California Institute of Technology,

Pasadena 91109, California, U.S.A.

ABSTRACT. High-resolution radar images of Moreno Glaciar, Argentina, acquired by the Shuttle Imaging Radar C (SIR-C) on October 9 and 10 1994, at 24-cm wavelength (L-band), are utilized to map the glacier velocity both interferometrically and using a novel feature tracking technique. The precision of the interferometric ice velocities is 1.8 cm d^{-1} (6 m a^{-1}). Feature tracking based on the phase correlation method measures ice velocity with a precision of 14 cm d^{-1} (50 m a^{-1}) with image data acquired one day apart, at a 6-m sample spacing. Strain rates are measured with a precision of 10^{-4} d^{-1} at a 240-m sample spacing with feature tracking, and 10^{-5} d^{-1} with interferometry. Feature tracking is less precise than radar interferometry, but it performs better in areas of rapid flow, is more robust to temporal changes in glacier scattering, and measures the glacier velocity in two dimensions with only one image pair. Using this technique, we find that Moreno Glaciar flows at 400 m a^{-1} in the terminal valley and 800 m a^{-1} at the calving front, in agreement with velocities recorded a decade ago. Assuming steady-state flow conditions and a constant longitudinal slope in glacier thickness, the vertical strain rates measured by SIR-C are combined with prior data on mass ablation to estimate the glacier thickness and ice discharge. The calculated discharge is $0.6 \pm 0.2 \text{ km}^3 \text{ ice a}^{-1}$ at 300 m elevation, $1.1 \pm 0.2 \text{ km}^3 \text{ ice a}^{-1}$ at the equilibrium line elevation (1,150m), yielding a balance accumulation of $6 \pm 1 \text{ m ice a}^{-1}$.

INTRODUCTION¹

The Patagonia icefields are located at the south-western tip of south America and consist of the northern icefield (Hielo Patagonico Norte) and the southern icefield (Hielo Patagonico Sur, HPS) (Fig. 1). Little glaciological information exists about these icefields although they represent one of the largest ice mass in the world and the largest temperate ice mass in the southern hemisphere (Warren and Sudgen, 1993).

Satellite imagery is naturally suited to the study of such regions. Landsat TM imagery has been used for large scale inventory of the icefields (Aniya and others, 1996), but the range of applications of these data is limited. Only one cloud-free set of images of the entire icefield has been available since the inception of the Landsat satellite.

Imaging radars are better adapted to the condition of these regions because they operate independent of cloud cover and solar illumination. In addition, when used interferometrically, imaging radars can yield precise information on surface topography and ice velocity of entire icefields.

Radar coverage of the Patagonia icefields started in the 1990's with the Japanese JERS-1 radar, an L-band (24 cm wavelength) imaging radar system, which imaged various portions of the icefields in late 1993 early 1994. The data quality was judged to be poor by Aniya and Naruse (1995) due to the lack of image contrast at the ice margin. The long time separation between repeat-pass JERS-1 acquisitions (24 days) also severely limits the possibility of interferometric analysis of the icefields. In March and October 1994, the NASA/Jet Propulsion Laboratory Shuttle Imaging Radar C (SIR-C) provided the first three-frequency, interferometric images of selected portions of the icefields (Forster and others, 1997; Rignot

¹Corresponding Author: Eric Rignot, Jet Propulsion Laboratory, Mail Stop 300-235, 4800 Oak Grove Drive, Pasadena CA 91109-8099, U.S.A; Ph +1 818 354-1640; E-mail: eric@adelie.jpl.nasa.gov; Fax: +1 818 354-0495

and others, 1996a and b; Rott and others, 1998) and a nearly complete multi-channel coverage of HPS (Forster and others, 1996). Finally, in late 1995, the Earth Remote Sensing satellite (ERS-1 and 2) provided a comprehensive, repeated interferometric coverage of the icefields.

Radar interferometry has its limitations. If the glacier surface changes too significantly in between successive imaging acquisitions, for instance due to surface melting, the distribution of scatterers at the surface of the glacier is altered, the fading pattern of the radar signal is modified, and the phase coherence of the radar signal is no longer preserved, making it impossible to measure glacier velocities interferometrically. Similarly, phase coherence is destroyed when the glacier deformation within an image pixel exceeds half the radar wavelength, for instance due to large strain rates along shear margins.

In areas of excessive glacier weathering and/or deformation where radar interferometry is not always successful, we propose a novel and complementary technique of data analysis for measuring ice velocity. This technique is apperented to the feature tracking algorithm used with success on visible satellite imagery (Bindshadler and Scambos, 1991) and more recently on repeat-pass ERS radar imagery (Fahnestock and others, 1993). There are however significant differences between the "Landsat" technique and the one presented here. The new technique, based on the so-called "phase correlation method" (Schaum and Hugh, 1991), is intrinsically more precise, requires no recognizable image features at the glacier surface, and operates with image data acquired just a few days apart as in the case of radar interferometry.

An example application of this feature tracking technique is presented here in the case of Moreno Glaciar, a major outlet glacier of HPS, which was imaged repeatedly for interferometric applications in October 1994 by SIR-C (Fig. 1). The data set acquired by SIR-C over Moreno Glaciar is utilized to test the precision and limitation of the feature tracking

technique by comparing it with radar interferometry, and establish the level of synergy and complementarity between the two techniques. The results are subsequently employed to infer first-order estimates of the ice volume discharge and balance accumulation of Moreno Glaciär assuming stable ice flow conditions.

STUDY AREA

Moreno Glaciär, officially known as Glaciär Perito Moreno, occupies an area of 257 km², 30 km in length and 4 km wide in the terminal valley, with an accumulation area of 182 km² (Aniya and Skvarca, 1992). The glacier flows eastward from the eastern edge of HPS and calves into Lago Argentino where it divides the channel into the Canal de los Tempanos to the north and the Brazo Rico to the south. The glacier is well-known for repeatedly damming up the Brazo Rico by reaching the opposite bank of the channel. Moreno Glaciär is one of the few Patagonian glaciers to be reached easily, and there is an abundance of historical and glaciological data on that glacier (Aniya and Skvarca, 1992). Historical data on the position of the terminus suggest that the glacier has been more or less in steady state during the last century. This conclusion is supported by measurements of changes in surface elevation along a 3-km long area 5 km from the glacier front which revealed little change in ice thickness over a two-year period (Naruse and Aniya, 1992). The glacier velocity, first measured forty years ago by Raffo and others (1953) along a transverse profile 5-6 km from the glacier front, was re-measured at 11 locations in 1984 (Naruse and others, 1992).

Moreno Glaciär was imaged on October 7, 9 and 10, 1994 by NASA's SIR-C on-board the United States Space Shuttle Endeavour at both C- ($\lambda = 5.67$ cm) and L-band (24.23 cm) frequency, with vertical transmit and receive polarization, at an exact repeat-pass time interval of 23.618 hours (Fig. 2). Only the analysis of the L-band data is discussed here as the C-band data did not yield useful interferometric products due to the low phase coherence of the signal. SIR-C illuminated the scene at an incidence angle of 34.37° away from vertical.

The image pixel spacing is 3.33 m in slant-range (cross-track or line-of-sight direction), which is equivalent to 5.9 m in ground-range (ground-range = slant-range/sine(34.37°)).

METHODS

Interferometry

Repeat-pass radar interferometry measures surface deformation at the millimeter scale from the phase difference between radar signals collected on successive tracks over the same surface element (e.g., Gabriel and others, 1989). The geometry of the interferometer is presented in Fig. 3a. The interferometric phase for a point M on the ground is

$$\delta\phi = \frac{4\pi}{\lambda}[S_1M - S_2M] \quad (1)$$

where λ is the radar wavelength, S_1M and S_2M are the optical paths from M to the successive positions of the satellite S_1 and S_2 , and S_1S_2 is the interferometric baseline, B . To produce an interferogram, the complex radar images (meaning amplitude and phase of the radar signal expressed as a complex number) are co-registered with sub-pixel precision, and a raw interferogram (here oversampled by a factor of 2) is formed by computing the cross-product of the registered complex images. The interferogram is then spatially averaged using a Hamming window (8 x 8 image pixels in size) and a compensation of the local phase slope which preserves the local fringe rate (Michel, 1997). Taking into account phase slope is crucial in areas of high shear strain (for instance along the shear margins of a glacier) to preserve phase coherence during spatial averaging.

The interferometric phase, $\delta\phi$, is related to the orbital parameters (interferometric baseline, imaging angle, etc.), the surface topography, and the surface deformation (Zebker and others, 1994). The topography component of the signal may be removed using a prior-determined digital elevation model of the area or by combining two successive interferograms (Gabriel and others, 1989). Here, the interferometric baseline was only a few tens of me-

ters, so surface topography had a negligible influence on the signal measured from a single interferogram.

An image of the temporal coherence of the phase, ρ , is obtained from the magnitude of the normalized cross-products. Phase coherence determines the statistical noise of the interferometric phase,

$$\sigma_{\delta\phi} = \frac{1}{\sqrt{2N}} \frac{\sqrt{1-\rho^2}}{\rho}, \quad (2)$$

where N (here equal to 16) is the number of independent averaged samples used to generate the interferogram (Rodriguez and Martin, 1992). The uncertainty in glacier velocity measured along slant range is

$$\sigma_v = \frac{\lambda}{4\pi} \sigma_{\delta\phi} \quad (3)$$

Phase coherence varies spatially, and so is σ_v . With $\rho = 0.4$, a typical value for the SIR-C data, we have $\sigma_v = 0.8 \text{ cm d}^{-1}$ in slant range, which is equivalent to 1.4 cm d^{-1} in ground range.

Image Offsets

Surface velocity may also be derived from the correlation peak of the image amplitudes. The method is limited in precision by the size of the image pixels (the precision of radar interferometry is limited by the size of the observing radar wavelength), but it provides two-dimensional vector displacements (one-dimensional cross-track displacements only for radar interferometry) and is intrinsically more robust to temporal decorrelation of the radar signal because it relies on the image intensity (phase information only for interferometry).

Along slant range, the range offsets are due to the glacier velocity along that direction, combined with a stereoscopic effect of the baseline which yields an elevation dependent bias in range position. For a point M of the scene, the slant-range offset, δu , expressed in pixel

units, is

$$\delta u = R_r[(S_1 M - S_1 O_1) - (S_2 M - S_2 O_2)] \quad (4)$$

where O_1 and O_2 are the ground-range positions corresponding to M in image 1 and 2, respectively (Fig. 3a), and R_r is the pixel spacing in slant range.

For the same point M , the corresponding position S of the synthetic antenna at the time of imaging of M is the one which minimizes the distance MS . The velocity vectors, V_1 and V_2 , of the successive orbits of the satellite are not necessarily colinear (Fig. 3b). The angle, $\delta\alpha$, between the two vectors in the plane of incidence produces an elevation-dependent azimuth offset, δv , which, for a non-moving area, is expressed in pixel units as

$$\delta v = \frac{z \sin(\delta\alpha)}{R_z} - [1 - \cos(\delta\alpha)] l + \delta v_o \quad (5)$$

where l is the line number with reference to the first line of the reference radar scene, R_z is the azimuth or line spacing, z is the surface elevation, and δv_o is a constant offset. The first term on the right hand side of Eq. (5) is elevation dependent. The second term produces an azimuth ramp in the offset field.

To obtain reliable estimates of the glacier velocity, the image offsets, δu and δv , must be determined with sub-pixel precision. Sub-pixel precision image registration is also required to form radar interferograms since the characteristic size of the fading pattern is of the order of 1 to 1.5 pixels. To compute the offsets with sub-pixel precision from the amplitude data, we use the phase correlation method of Schaum and Hugh (1991). The deformation between the two images is approximated by a translation within Hanning windows 32 x 32 pixels in size. If \mathbf{a} and \mathbf{b} denote the amplitudes of two images translated by an amount δu in the range direction and δv is the azimuth direction, the Fourier transforms of \mathbf{a} and \mathbf{b} verify

$$\bar{b}(\mu, \nu) = \bar{a}(\mu, \nu) \exp [-2 \pi j (\mu \delta u + \nu \delta v)] \quad (6)$$

where μ and ν are, respectively, the spatial frequencies along range and azimuth. We isolate the phase shift by computing

$$\bar{C}(\mu, \nu) = \frac{\bar{a} \bar{b}^*}{|\bar{a} \bar{b}^*|} = \exp [2 \pi j (\mu \delta u + \nu \delta v)] \quad (7)$$

The inverse Fourier transform of \bar{C} is a Dirac function, δ , located at a position $(\delta u, \delta v)$

$$C(\mu, \nu) = \delta(\delta u, \delta v) \quad (8)$$

The normalization of $\bar{a} \bar{b}^*$ in Eq. (7) is a key feature of the phase correlation method which is responsible for the narrow shape of the correlation peak and an enhancement of its signal to noise ratio (SNR).

The numerical Fourier transform of the images leads to the determination of the correlation peak in pixel units. The SNR of the correlation peak is not optimum because of the non-overlapping areas of **a** and **b**, non-linear deformations associated with topography and velocity gradients within the sliding window, and changes in fading pattern (which are responsible for phase decorrelation). To reduce the effect of non-overlapping areas, we first evaluate the integer shift between the two images using the peak value of C , extract two new sub-images 16 x 16 pixels in size so that the non-overlapping areas do not exceed one pixel in size, and search again for the position of the correlation peak. A sub-pixel position of the correlation peak is then estimated as the barycenter (or weighted average) of the peak using

$$\begin{aligned} \delta u &= \frac{\sum_{(k, l) \in V} k C^2(k, l)}{\sum_{(k, l) \in V} C^2(k, l)} \\ \delta v &= \frac{\sum_{(k, l) \in V} l C^2(k, l)}{\sum_{(k, l) \in V} C^2(k, l)} \end{aligned} \quad (9)$$

where V is a 3 x 3 neighborhood of the correlation peak, and k and l are, respectively, the column and line indexes.

The conservation of the total energy of C

$$\sum_{(k, l) \in V} C^2(k, l) = 1 \quad (10)$$

allows for a practical evaluation of the signal to noise ratio (SNR) of the correlation peak in both range (u) and azimuth (v)

$$\begin{aligned} S_u &= \frac{\sum_{k \in V} \sum_l C^2(k, l)}{1 - \sum_{k \in V} \sum_l C^2(k, l)} \\ S_v &= \frac{\sum_{l \in V} \sum_k C^2(k, l)}{1 - \sum_{l \in V} \sum_k C^2(k, l)} \end{aligned} \quad (11)$$

The uncertainty in δu and δv is, respectively, a function of S_u and S_v .

To test the relationship between SNR and offset precision, we employed two computer-generated images, 1000 x 1000 pixels in size, with a known offset field (linearly varying offsets), calculated the offsets and SNRs as described above, and obtained the results shown in Fig. 4. As expected, low SNR values yield high offset errors. To obtain an offset precision of 1/30th of the pixel size, the SNR of the correlation peak needs to be better than 0.15.

The advantage of computing both S_u and S_v rather than only one "global" SNR is to limit the possibility of false matches associated with oblong correlation peaks, meaning a correlation peak which is narrow in one direction but broad in another, as recorded for instance in the presence of a train of crevasses. Here, a false match may be detected when either S_u or S_v is below a threshold (typically 0.15). The vector SNR measurements thereby procure more control on the quality of the vector offsets.

RESULTS

Velocity Estimates

The baseline and topography effects were removed automatically from both the SIR-C interferograms and the SIR-C offset map using an average fringe rate. This simplification

is justified by the short interferometric baseline of the data and the low glacier slope of Moreno Glaciär.

The L-band interferogram shown in Fig. 5 was unwrapped (meaning the fringes were counted from a zero reference to reconstitute absolute phase values) using Goldstein and others (1988)'s unwrapping technique, to yield the result shown in Fig. 6. Unwrapping could not be performed successfully near the glacier front and at high elevation because of low phase coherence in these regions. Feature tracking conversely performed well over the entire glacier to provide two-dimensional velocities, displayed on a regular grid in Fig. 7.

Eq. 1 and 4 show that the unwrapped phase, $\delta\phi$, and the range offset, δu , are linearly related via

$$\delta u = R_r \frac{4\pi}{\lambda} \delta\phi + \delta u_o \quad (12)$$

Fig. 8a and b show a comparison between the interferometric velocities and the slant-range image offsets measured along the transverse and longitudinal profiles shown in Fig. 6. Systematic errors introduced by topographic features and baseline errors have the same signature in both cases, so the difference between the two curves represents an unbiased comparison of the two techniques. The image offset method provides a comprehensive coverage of the glacier, whereas radar interferometry only works in the glacier lower reaches.

The average uncertainty in interferometric velocity is 1 cm d^{-1} based on the statistical noise of the interferometric phase (the error bar is too small to be visible in Fig. 8a and b), which translates into 1.8 cm d^{-1} of uncertainty in ground-range motion. The average difference between the offset velocity and the interferometry velocity is 8 cm d^{-1} in slant range, or 14 cm d^{-1} in ground range (50 m a^{-1}), which is equivalent to a precision of detection of the offsets of 1/30th of a pixel. In profile 2, the calculated offset error is larger along the glacier margins (up to $10\text{-}15 \text{ cm d}^{-1}$) because the SNR is lower. In general, the offsets remain within one calculated standard deviation of the interferometry measurements.

One exception is found along the northern margin of profile 2 where the offset precision is apparently overestimated.

More precise ice velocities may be obtained from feature tracking using data acquired with a longer time separation. The signal correlation may eventually decrease after a few days, so there is an optimal time period for our technique to be used. More accurate velocity measurements may also be obtained by using larger-size averaging windows when computing the image correlation peak, at the expense of spatial resolution.

Phase unwrapping fails when phase coherence drops below about 0.2, in which case ice velocity cannot be measured interferometrically. Feature tracking becomes unreliable when the correlation peak SNR drops below 0.06, which corresponds to an offset error of 0.5 pixels (Fig. 4). Phase coherence and correlation peak SNR are independent variables, so the performance of feature tracking cannot be predicted in regions where phase coherence is low. The phase correlation method, however, typically works best where radar interferometry breaks down, for instance in areas experiencing significant weathering (ablation or precipitation) and/or large glacier deformation.

Comparison with prior measurements

Using an electronic distance meter, Naruse and others (1992) measured the glacier velocity at 11 points and derived vertical strain rates. Half of the measurements were collected along a transverse profile located 4 km from the ice front, running from the right bank of the glacier to its middle section. The others measurements were collected along a longitudinal profile about 2 km from the right margin, and 4 km from the ice front. Fig. 9 compares their results with the SIR-C measurements. The comparison shows no significant change in ice velocity between November 1990 and October 1994, except perhaps near the ice front where Naruse and others (1992)'s velocity measurements are expected to be least precise

or 12.2 m ice a⁻¹; and \dot{B} to vary with surface elevation with a gradient of 0.015 a⁻¹. The glacier net balance is therefore 13 m a⁻¹ ice volume at 300 m elevation, or 3.56 cm ice d⁻¹.

The slope in glacier thickness, $\frac{\partial H}{\partial X}$, not known from prior field experiments, is assumed to be constant across the glacier width as well as in the longitudinal flow direction. To estimate its value, we consider the positions along the 300-m profile for which $\dot{\epsilon}_z$ is zero to obtain

$$\frac{\partial H}{\partial X} = \left(\frac{\dot{B}}{V_x} \right)_{\dot{\epsilon}_z=0} \quad (15)$$

The resulting thickness profile is shown in Fig .11. The precision is 30 percent, or 200 m, based on the uncertainty in strain rate, velocity and ablation data. The error in ice thickness could be larger if our assumption of constant thickness slope is unrealistic.

The ice volume flux, Φ , is deduced using

$$\Phi = \int \mathbf{V}(\mathbf{x}) \cdot \mathbf{n}(\mathbf{x}) H(x) dx \quad (16)$$

along the 300-m contour, where \mathbf{n} is the normal to the contour and \mathbf{V} is the ice velocity vector (Fig. 12). We assume that the glacier surface velocity represents a reliable measure of the vertically-integrated velocity, meaning that basal sliding is significant close to the glacier front. The result is an ice flux of $0.6 \pm 0.2 \text{ km}^3 \text{ ice a}^{-1}$ at 300 m elevation. From the gradient in melt rate measured by Naruse and others (1995) and the published topographic map of the glacier, we calculate an ice flux at the equilibrium line elevation (1,150m) of $1.1 \pm 0.2 \text{ km}^3 \text{ ice a}^{-1}$. Averaged over the entire accumulation area (182 km^2), the glacier discharge yields a balance accumulation of $6 \pm 1 \text{ m ice a}^{-1}$.

An ice core drilled at 2680 m elevation, near the top of the accumulation area of Moreno Glaciar (Aristarain and Delmas, 1993), yielded an accumulation rate of 1.2 m a⁻¹ water equivalent, deemed too low by Naruse and others (1995). Using published precipitation maps in Chile, Naruse and others (1995) suggested instead that snow accumulation reaches

8 m a⁻¹ at 2000 m elevation, linearly decreasing with elevation. They quote a mean precipitation over the eastern ice-covered areas of 6.4 m a⁻¹. Our result, which represents a balance accumulation over the entire accumulation area of Moreno Glaciar, is consistent with their interpretation and close to their quoted estimate of mean precipitation along the eastern flank of HPS.

More recently, Rott and others (1998) conducted field surveys on Moreno Glaciar which produced a complete ice thickness seismic profile a few kms above the 300-m elevation contour. Their measured ice thickness averaged 440 m, compared to 490 m in our inversion. The retrieved thickness profile has however a more pronounced parabolic shape than that shown in Fig. 12. Rott and others (1998) deduced an annual net accumulation of 5.54 ± 0.5 m water a⁻¹ from their data, which is within the error bounds of the estimate obtained here.

CONCLUSIONS

The study demonstrates the possibility of obtaining accurate ice velocities and strain rates from feature tracking of satellite radar images acquired with a short repeat-pass time interval compatible with that required for radar interferometry applications. Feature tracking provides two-dimensional vector velocities, over a large range of glacier conditions and changes in glacier scattering. Current imaging radar systems available for interferometric applications over glaciated terrain, such as ERS and JERS, do not offer repeat-pass cycles that are short enough for measuring velocities of fast-moving outlet glaciers in Patagonia, Alaska, or along the western and eastern coasts of Greenland. Feature tracking based on the phase correlation method may in that case be considered as an indispensable complement to radar interferometry.

In the case of the ERS system, pixel spacing is 20 m in ground range (7.9 m along the

line of sight); and 4 m in azimuth. Extrapolation of the SIR-C results to the case of ERS suggests that feature tracking using the phase correlation method will measure ice velocity in azimuth with a precision of 13 cm d^{-1} (49 m a^{-1}), and 67 cm d^{-1} (240 m a^{-1}) in ground range. This level of precision should be sufficient to provide first order estimates of the ice velocity of fast-moving ice fronts.

Another important potential utilization of the technique is to measure ice-shelf velocities along track, independent of the effect of ocean tides on the ice shelf.

ACKNOWLEDGEMENTS

This work was partially performed at the Jet Propulsion Laboratory, California Institute of Technology, under a contract with the National Aeronautics and Space Administration. We thank J. Taboury of Institut d'Optique Theorique et Appliquee, Orsay, France and J.P. Avouac, Laboratoire de Detection et de Geophysique, Bruyeres le chatel, France for useful discussions during the course of this project.

REFERENCES

Aniya, M., H. sato, R. Naruse, P. Skvarca and G. Casassa. 1996. The use of satellite and airborne imagery to inventory outlet glaciers of the southern Patagonia icefield, South America, *Photogram. Eng. Rem. Sens.* **62**(12), 1361-1369.

Aniya, M. and R. Naruse. 1995. A study of glacier variations in Patagonia, South America, utilizing SAR images, *Final Report of JERS-1/ERS-1 system verification program, vol. II*, Ministry of International Trade and Industry, NASDA, Tokyo, Japan, 555-562.

Aniya, M. and P. Skvarca. 1992. Characteristics and variations of Upsala and Moreno glaciers, southern Patagonia. *Bull. Glacier Res.*, **10**, 39-53.

Aristarain, A.J. and R.J. Delmas. 1993. Firn-core study from the southern Patagonia ice cap, South America, *J. Glaciol.* **39**(132), 249–254.

Bindschadler, R.A. and T.A. Scambos. 1991. Satellite-image-derived velocity field of Antarctic ice stream, *Science* **252** 242–246.

Fahnestock, M., R.A. Bindschadler, R. Kwok, and K. Jezek. 1993. Greenland ice-sheet surface-properties and ice dynamics from ERS-1 SAR imagery, *Science* **262** (5139), 1530–1534.

Forster, R.R., E. Rignot, B.L. Isacks and K. Jezek. 1997. Interferometric radar observations of the Hielo Patagonico Sur, Chile, *J. Glaciol.*, subm.

Forster, R.R., B.L. Isacks and S.B. Das. 1996. Shuttle imaging radar (SIR-C/X-SAR) reveals near-surface properties of the south Patagonian icefield, *J. Geophys. Res.* **101** (E10), 23,169–23,180.

Gabriel, A.K., R.M. Goldstein and H.A. Zebker. 1989. Mapping small elevation changes over large areas: differential interferometry, *J. Geophys. Res.* , **94** (B7), 9183–9191.

Goldstein, R.M., H.A. Zebker and C.L. Werner. 1988. Satellite radar interferometry : two-dimensional phase unwrapping. *Radio Sci.*, **23** (4), 713–720.

Michel, R. 1997. Les mesures de mouvements par imagerie SAR et leur exploitation en glaciologie et en sismotectonique, Thèse, Université PARIS XI, Dec. 1997.

Naruse, R., P. Skarca, T. Kadota, and Ken Koizumi. 1992. Flow of Upsala and Moreno glaciers, southern Patagonia. *Bull. Glacier Res.*, **10**, 55–62.

Naruse, R., M. Aniya, P. Skvarca and G. Casassa. 1995. Recent variations of calving

glaciers in Patagonia, South America, revealed by ground surveys, satellite-data analyses and numerical experiments, *Ann. Glaciol.* **21**, 297–303.

Naruse, R. and M. Aniya. 1992. Outline of Glacier Research Project in Patagonia, 1990, *Bull Glacier Res.* **10**, 31–38.

Paterson, W.S.B. 1994. *The physics of glaciers. Third Edition.* Oxford, etc., Pergamon Press.

Raffo, J.M., B.S. Colquhoun and M.E. Madejski. 1953. Glaciar Moreno. Direccion General del Servicio Meteorologico Nacional, Buenos Aires, Serie Hidrometeorologica Publicacion No. 9, 293–341.

Rignot, E. , R. Forster and B. Isacks. 1996a. Mapping of glacial motion and surface topography of Hielo Patagonico Norte, Chile, using Satellite SAR L-band Interferometry Data. *Ann. Glaciol.* **23**, 209–216.

Rignot, E. , R. Forster and B. Isacks. 1996b. Interferometric radar observations of Glaciar San Rafael, Chile, *J. Glaciol.* **42**(141), 279–291.

Rodriguez, E. and J. Martin. 1992. Theory and design of interferometric synthetic-aperture radars, *IEE Proc. Ser. F* **129**(2), 147–159.

Rott, H., M. Stuefer, A. Siegel, P. Skvarca and A. Eckstaller. 1998. Mass fluxes and dynamics of Moreno Glacier, Southern Patagonia Icefield, *Geophys. Res. Lett.*, in press.

Scambos, T.A., M.J. Dutkiewicz, J.C. Wilson and R.A. Bindshadler. 1992. Applications of image cross-correlation to the measurement of glacier velocity using satellite image data, *Rem. Sens. Environ.* **42**, 177–186.

Schaum, A. and M. McHugh. 1991. Analytic method of image registration : displacement estimation and resampling, Report of the Naval Research Laboratory, NRL Report No. 9298.

Warren, C.R. and D.E. Sudgen. 1993. The Patagonian icefields: a glaciological review, *Arctic Alp. Res.* **25**(4), 316-331.

Zebker, H.A., P.A. Rosen, R.M. Goldstein, C. Werner and A. Gabriel. 1994. On the derivation of coseismic displacement fields using differential radar interferometry: the Landers Earthquake. *J. Geophys. Res.*, **99** (B10), 19,617-19,634.

Figure Captions

FIG 1. Location map of Moreno Glaciar, Argentina, in the Southern Patagonia Icefield (Hielo Patagonico Sur). The black box shows the approximate location of the SIR-C frame discussed in the paper. The shaded areas represent the icefields.

FIG 2. Radar amplitude image of Moreno Glaciar acquired on October 9, 1994 by the Shuttle Imaging Radar C instrument at L-band frequency (24 cm wavelength), vertical transmit and receive polarization, at a mean incidence angle of 35 degrees. The radar was flying from left to right, illuminating the ground from its left. The white box delineates the area of interest discussed in subsequent figures.

FIG 3. Radar imaging geometry for (a) cross-track interferometry between positions S_1 and S_2 of the radar antenna illuminating a point M on the ground at elevation z from an altitude h , and where B is the interferometric baseline; and (b) along-track feature tracking of a point M at elevation z . The velocity vectors, V_1 and V_2 , of the two successive positions of the satellite form an angle $\delta\alpha$ in the vertical plane. The dotted circles in (a) and (b) denote an axis coming out of the plane of the figure toward the viewer. R_z is the spatial resolution along track or azimuth.

FIG 4. Precision of the image offsets expressed in pixel spacing as a function of the signal to noise ratio (SNR) of the image correlation peak expressed in linear unit in the case of computer-generated test data.

FIG 5. Radar interferogram of Moreno Glaciar, obtained by combining data acquired on Oct. 9 and 10 1994 by the SIR-C instrument at L-band frequency. Each fringe, or 360 deg. variation in phase, going from blue to purple; yellow and blue again, represents a 12 cm displacement of the glacier surface in the line of sight of the radar.

FIG. 6. Unwrapped radar interferogram (shown in Fig. 5) of Moreno Glaciar, and location of profiles 1 and 2 used for the comparison between interferometry and feature tracking, and of the 300-m elevation contour line used to estimate ice discharge.

FIG. 7. Ice velocity vector of Moreno Glaciar within the area delineated with a white box in Fig. 2 and derived from feature tracking. Flow vectors are overlaid on the radar brightness of the scene at L-band frequency. The spacing between flow vectors is 320 m.

FIG. 8. Comparison of feature-tracking velocities measured in slant range with radar-interferometry estimates along (a) longitudinal profile 1 in Fig. 6, and (b) transverse profile 2 in Fig. 6. Error bars correspond to one standard deviation in ice velocity. Interferometric measurements plotted on the horizontal axis (zero velocity) correspond to data points for which phase unwrapping was not successful and hence ice velocity could not be estimated interferometrically. Positions are measured in reference to the south bank of the glacier for profile 1, and the glacier terminus for profile 2.

FIG. 9. Comparison between the velocities measured by Naruse and others (1992) and the SIR-C feature tracking results along (a) a longitudinal profile, and (b) a transverse profile (See text for location of profiles). Error bars from Naruse and others (1992)' data are not available.

FIG. 10. Strain rate (per day) of Moreno Glaciar along the 300-m elevation contour profile in Fig. 6, along the range direction (both interferometry and feature tracking (called offsets)), azimuth (offsets only), and (c) vertical (offsets only). Each value is calculated using a 240-m spacing, and the results are interpolated every 100 m.

FIG. 11. Ice thickness of Moreno Glaciar at 300-m elevation deduced from mass conservation assuming steady flow conditions and using the vertical strain rates measured with SIR-C combined with prior data on mass ablation (Naruse and others, 1995). The precision

in ice thickness is 200 m, worsening along the side margins due to a lower signal to noise ratio. The first point of the profile (distance = 0) is a singular point in the inversion which produces an erroneous estimation of ice thickness.

FIG. 12. Ice velocity of Moreno Glaciar in the direction perpendicular to the 300-m elevation contour profile shown in Fig. 6 and derived from feature tracking. Error bars correspond to one standard deviation in ice velocity.

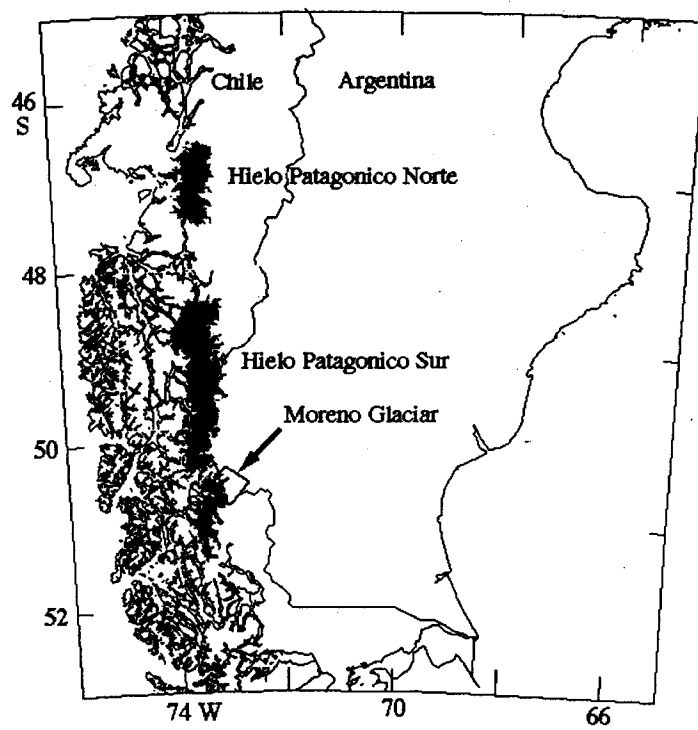


Fig. 1

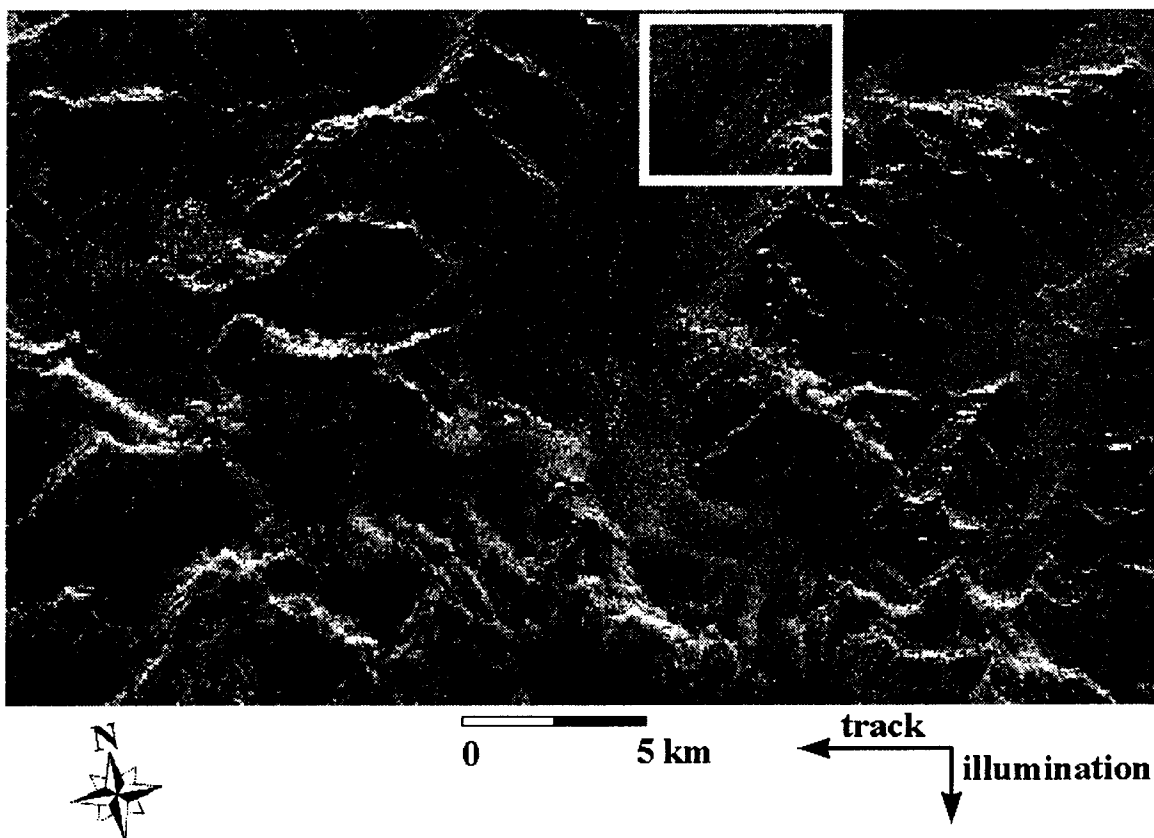
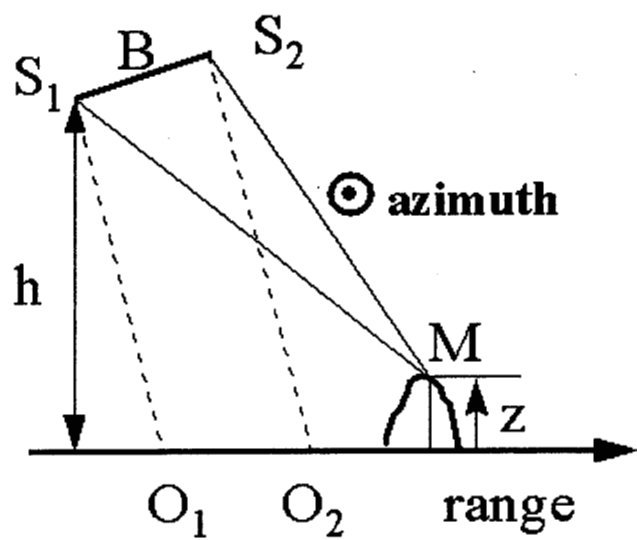
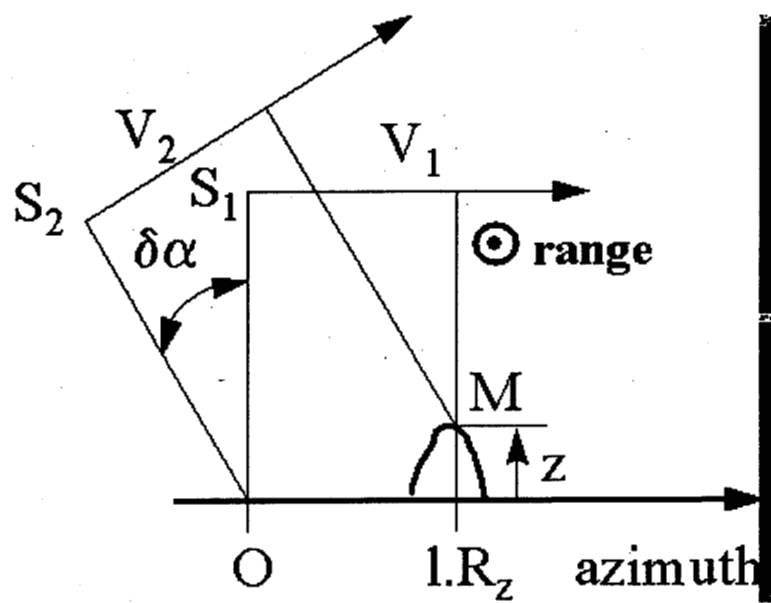


Fig. 2



(a)



(b)

Fig. 3

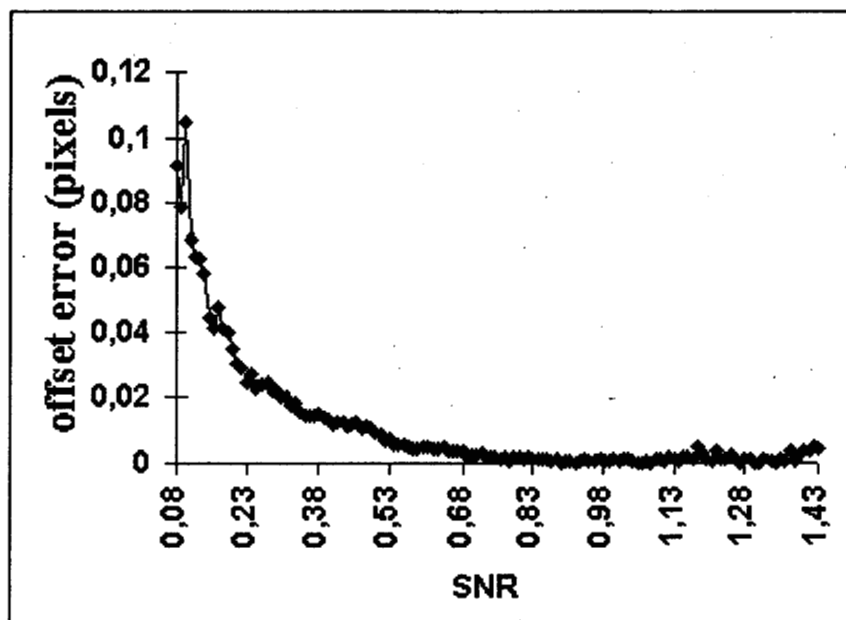


Fig. 4



0



2π



0

1km



track



illumination

Fig. 5

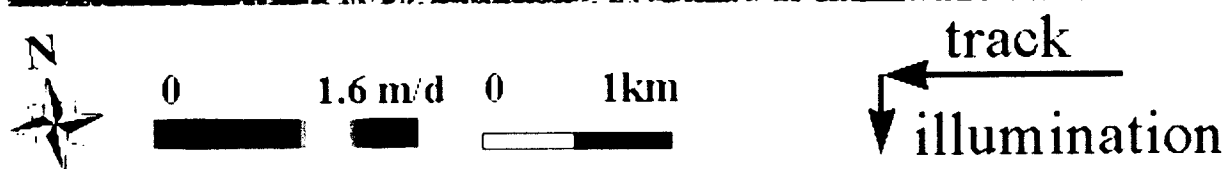


Fig. 6

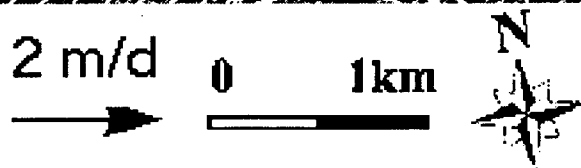
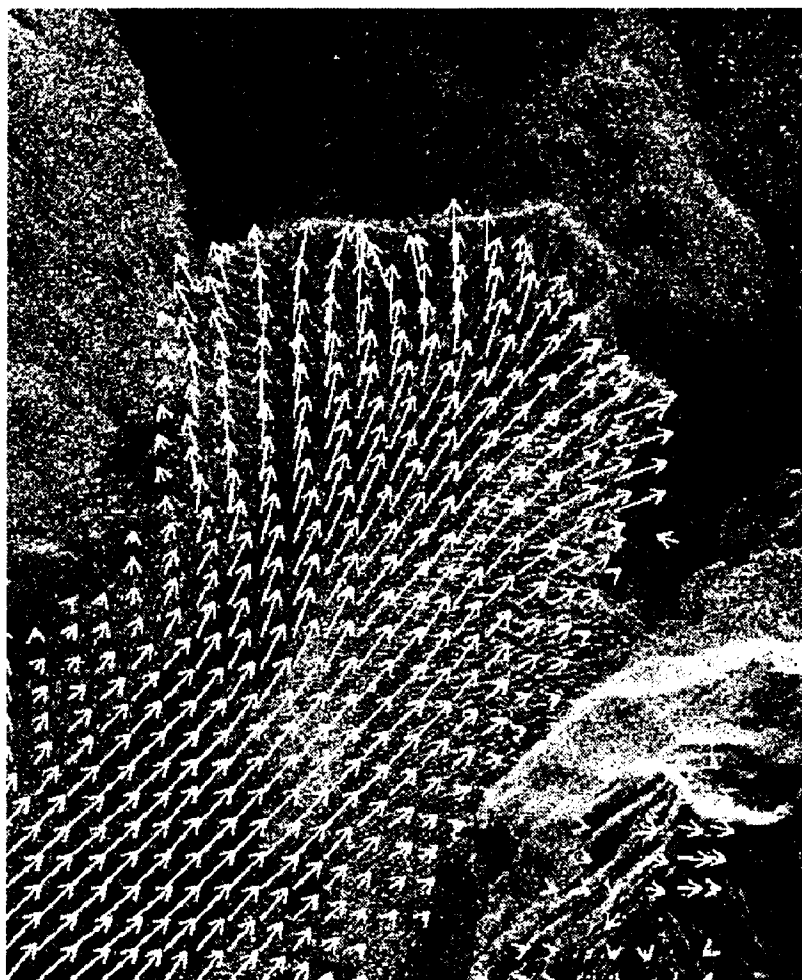


Fig. 7

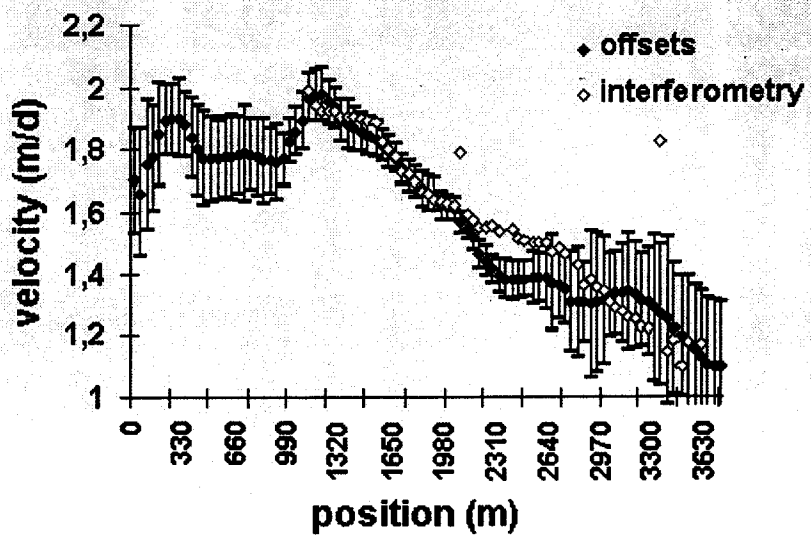
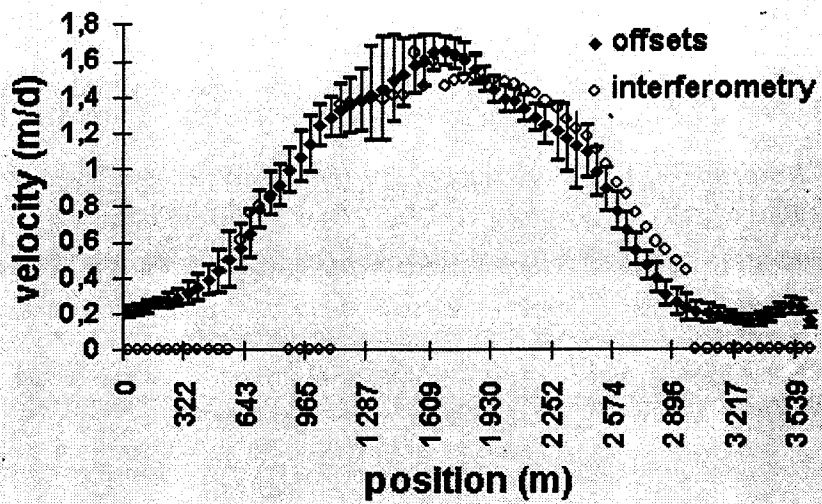
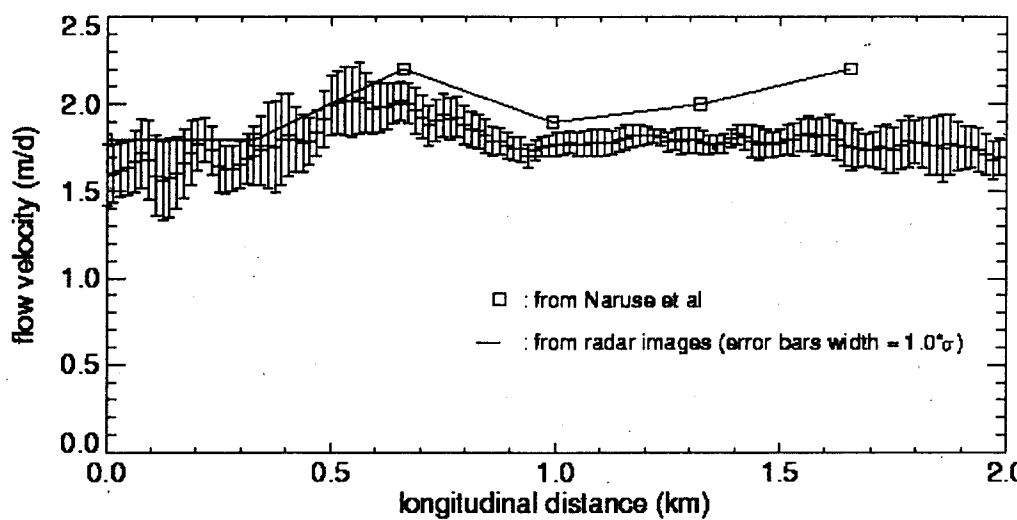
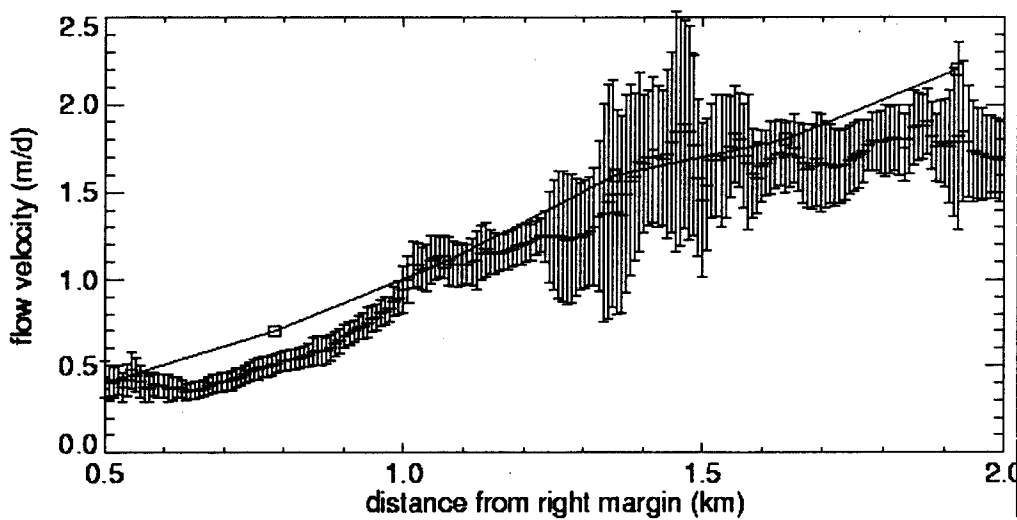


Fig. 8



(a)



(b)

Fig. 9

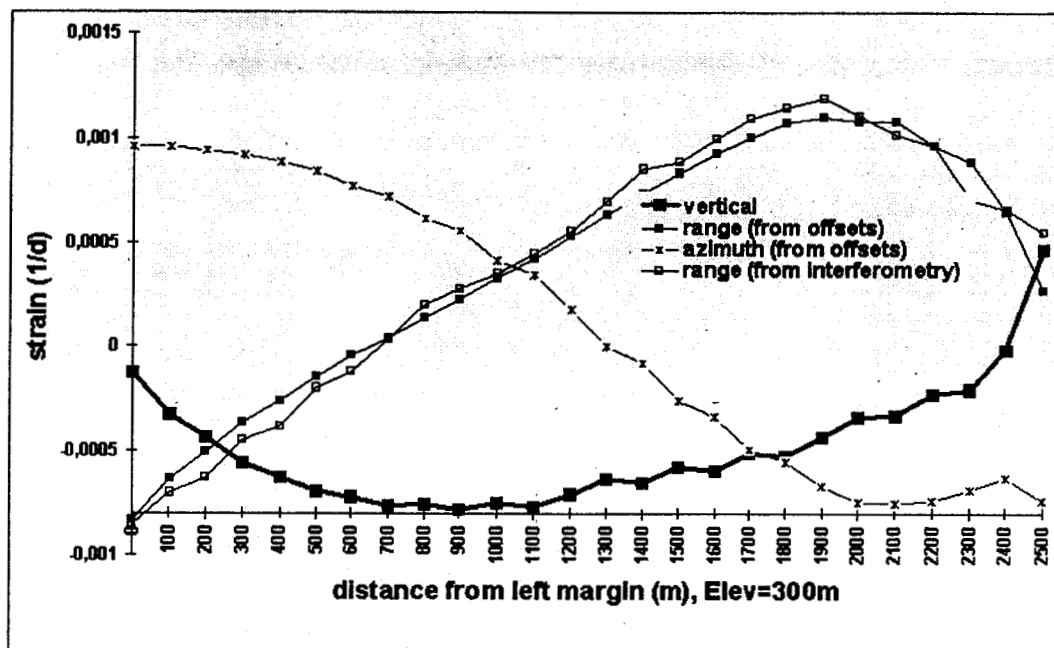


Fig. 10

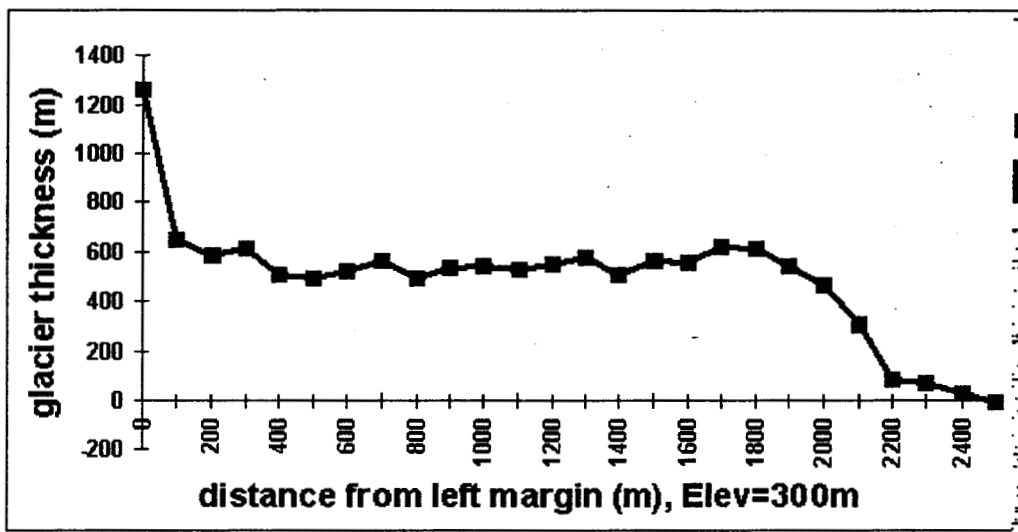


Fig. 11

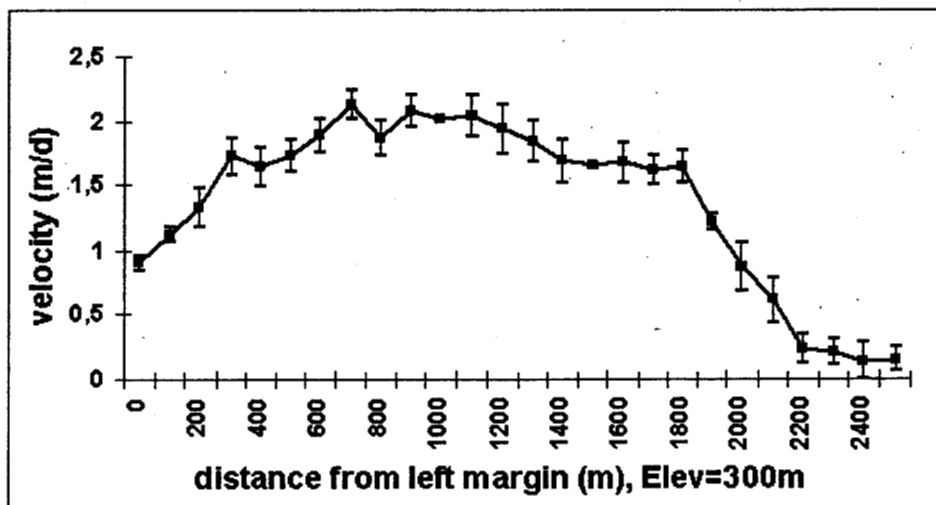


Fig. 12